Wear 400–401 (2018) 156–168

Contents lists available at ScienceDirect

Wear

journal homepage: www.elsevier.com/locate/wear

Evaluation of wear in rolling contact tests by means of 2D image analysis

I. Bodini*, C. Petrogalli, M. Faccoli, M. Lancini, S. Pasinetti, G. Sansoni, F. Docchio, A. Mazzù

Department of Mechanical and Industrial Engineering, via Branze, 38, 25123 Brescia, Italy

ARTICLE INFO

Keywords:
Twin-disk tests
Wear
Image acquisition
Damage monitoring
Image processing

ABSTRACT

Twin-disk tests are an effective method to characterize the material response to rolling sliding contact, to reproduce the damage phenomena of real components at a laboratory scale in controlled working conditions. Usually the monitoring is performed by means of "gross" parameters, such as weight loss, coefficient of friction and Barkhausen noise, and micrographs of the sample sections, at the end of the test. Visual inspection of the sample contact surface at the macro-scale yields further information about the process under analysis. In twin-disk tests, the samples are visually inspected at predetermined steps, typically by acquiring the image of their surface when the samples are stationary. The availability of a system able to capture the images of the samples while they roll during the tests is of interest to better monitor the damage evolution. In this paper, we present the results of the experiments carried out to extract quantitative information from the images captured on railway wheel samples during rolling contact tests: suitable image processing has been designed with the objective of finding meaningful, synthetic indices for the monitoring and the interpretation of the wear process, also in relation to prior knowledge about the process. The experimental work was focused on the definition of the indices, on the analysis of their behavior on different steels, and on their usefulness to predict uneven wear during the tests on the test bench.

1. Introduction

Twin-disk tests allow to investigate the material response to rolling-sliding contact, as they are able to reproduce the damage phenomena of real components at a laboratory scale in controlled working conditions. Different damage mechanisms interacting and affecting each other, such as wear, Rolling Contact Fatigue (RCF), strain hardening, and ratcheting [1,2] may be observed in samples tested with a bi-disk apparatus. Recognizing and studying these phenomena is a key issue for material characterization. For this reason, bi-disk tests have been widely used to characterize materials for bearings, gears, railway wheels and rails [3,4].

Usually, monitoring is performed by means of "gross" parameters, such as weight loss, friction coefficient and Barkhausen noise, measured at predetermined steps of the test, also with the support of suitable models, specifically developed to understand the damage process and to predict its evolution. The analysis of the samples at the end of the test is mandatory to fully understand the damage process: this is carried out by cutting the sample, and by taking micrographs of the section, which allow the detection and the quantitative measurement of sub-surface cracks. In most cases, optical methods are used to perform this task, such as white light confocal microscopy [5] and scanning electron microscope (SEM) image analysis [6,7].

Visual inspection of the sample contact surface at the macro-scale yields further information about the process under analysis: small dips are often observed in the presence of wear, corrugations are typical of the onset of plastic strain, larger craters are visible when the fatigue process determines the removal of the material as a consequence of the propagation of surface cracks to a certain depth and then towards the surface. In twin-disk tests, the samples are visually inspected at predetermined steps, typically by acquiring the image of their surface in an off-line approach, when the samples are stationary, mostly for qualitative analysis and documentation of the process.

The availability of a system able to capture the images of the samples while rolling during the tests is of interest to better monitor the damage evolution. In particular, the possibility of preprogramming the cadence of the acquisition sessions and of the duration of each session, and the availability of an efficient image processing procedure, yielding quantitative information on the surface characteristics, can be strategic in view of correlating the information with prior knowledge about the process.

In previous works of the authors [8,9], disk-shaped rail-wheel couples were tested on a twin-disk machine, and microscope analysis was performed at the end of the test. Subsequent versions of the testing apparatus have been presented [10,11] where vibrations and torque of the test bench are monitored, to provide continuous wear observation

* Corresponding author.
E-mail address: ileana.bodini@unibs.it (I. Bodini).

https://doi.org/10.1016/j.wear.2017.12.023
Received 2 June 2017; Received in revised form 18 December 2017; Accepted 30 December 2017
Available online 01 January 2018

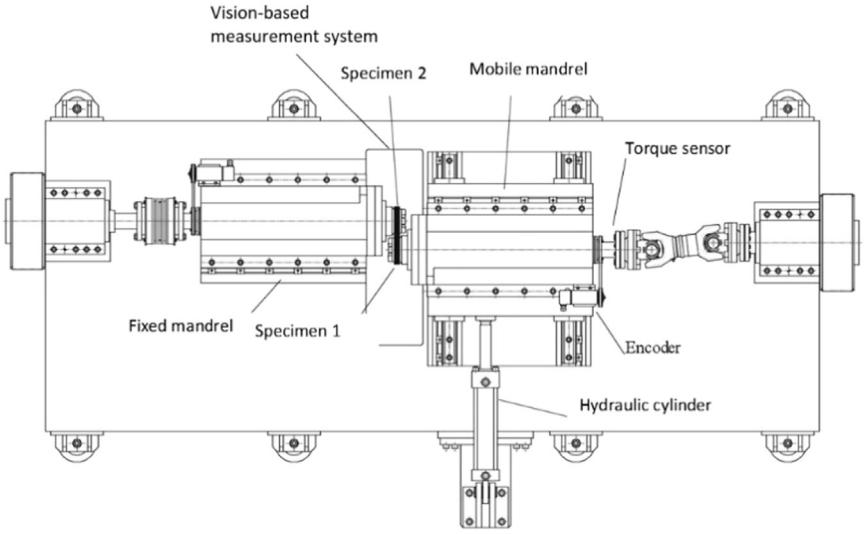

Fig. 1. Schematic drawing of the Twin-disk test set-up.

and to early detect RCF cracks. To further improve the apparatus, a novel design of a camera system was required for acquiring the specimens, with the aim of (i) documenting the tests, (ii) adding quantitative analysis of the surface topography evolution to the qualitative observation possible through mere visual inspection, and (iii) detecting uneven damage of the samples due to incorrect mounting, (the so called "polygonal" effect), for timely test stop [12].

The developed vision system acquires good quality images even at the highest specimen rotation speeds, thanks to the use of a high-speed video camera, and to the design of a suitable illumination. Acquisition triggering is available to provide user-selectable duration of the acquisition sessions and of the time separation between consecutive acquisitions. Image sequences are stored in video files for documentation purposes and subsequent analysis; unambiguous correlation between each image and the corresponding angular position of the rolling specimen is provided for all the images captured in each video. Suitable image analysis, exploiting the directional properties of the light, has been developed, to provide quantitative information on the surface topology evolution [13,14].

In the system, two diffused laser beams illuminate the rolling sample and the camera captures the light reflected back from the surface. The damage process consists of the removal of the sample material, which results into the formation of small valleys on the surface: each valley acts as a converging lens and results into a light spot at the video-camera sensor. During the damage process, the valleys change in their number, shape, dimension and orientation and induce a corresponding variation in the spot patterns captured at the image level. The image analysis approach focuses on detecting groups of connected, bright pixels (thereafter called 'particles') and on measuring their dimension, number and spatial orientation. With respect to other methods, such as those based on reflection models [15] and on super resolution image processing [16] (proposed for the analysis of single images in an off-line approach), the image analysis developed with our system is suitable for fast elaboration of the captured videos.

In this paper, the vision system was used in combination with the twin-disk machine in dry rolling contact tests. We present the results of the image analysis performed on the captured images with the aim of providing quantitative information of the evolution of the damage shared by four railway wheel steels. The emphasis is on the synthetic indices extracted from the patterns of particles in the captured images, on their behavior with the tested steels, and on their correlation with the weight loss exhibited by the tested samples.

In addition, we present the results of the image analysis carried out on a disk specimen made of the UIC 900A rail steel which underwent an 800 kcycles-long dry test against a wheel-specimen made of Superlos®, and became polygonal during the test. The ability of the optical system to monitor the surface topography evolution of the disk on an angle-dependent basis resulted in the possibility of detecting non-uniform damage of the rolling specimen.

2. The experimental apparatus

2.1. Twin-disk test bench and materials

A schematic drawing of the twin-disk bench is shown in Fig. 1: the specimens are positioned onto independent shafts, one of which can be displaced orthogonally to the shaft axis by a hydraulic cylinder that applies the imposed contact load. The rolling speed of the shafts is measured by encoders, and a load cell located at the piston head measures the contact load between specimens. The bench is equipped with a torque sensor positioned on the displaceable shaft, which can continuously acquire torque values at a synchronous sampling frequency of 5 kHz.

The measured torque signal is elaborated to obtain the friction coefficient between the specimens, by means of a procedure aimed at excluding the contribution of the shaft supporting bearings. During the first 300 cycles of each test, the two discs are pressed against each other and rotated with no relative tangential velocity, by means of a rolling speed control. The average toque value T_i recorded in this phase is assumed to be only due to the bearings and the discs' inertia. Then, the test phase begins and the relative rotation between the discs is allowed; the friction coefficient f is computed by subtracting T_i from the measured torque T and by dividing the result by the disc radius R and by the applied radial force F_r, as shown in Eq. (1):

$$f = \frac{T - T_i}{RF_r} \tag{1}$$

Four different wheel steels were investigated. The first steel, CLASS C (AAR M107/M208 2004), is widely used in North America. Two other steels, named SANDLOS® S and SANDLOS® H, are upgraded materials, type AAR CLASS C and AAR CLASS D modified, respectively. They have higher content of Mn and Si than ER8 and CLASS C and are micro-alloyed with V and Nb. The last two chemical elements are added intentionally, in accordance with maximum requirements (V $\leq$ 0.04% and Nb $\leq$ 0.05%), to improve the cyclic yield strength and fracture toughness in the wheel tread. SANDLOS® H has a higher content of V and Nb than SANDLOS® S. The rail steel was a 350 HT EN 13674-1. The fourth steel, ER8 (EN13262) is widely used in Europe. All steels are supplied by Lucchini RS. Their chemical composition and mechanical properties are reported in Table 1.

Table 1
Main chemical elements (wt%) and mechanical properties of the wheel and rail steels.

		CLASS C	SANDLOS® S	SANDLOS® H	ER8	350 HT
Chemical composition [wt%]	C	0.70	0.72	0.75	0.54	0.72
	Mn	0.78	0.80	0.80	0.75	1.04
	Si	0.34	0.87	0.87	0.34	0.30
	S	0.002	0.001	0.001	0.001	0.004
	P	0.009	0.010	0.006	0.009	0.015
Ultimate tensile stress [MPa]		1120	1180	1270	980	≥ 1175
Monotonic yield stress [MPa]		715	750	800	600	–
Elongation [%]		12	12	11	14	≥ 9
Hardness HB		355	347	354	283	345

Wheel and rail specimens were obtained from new real wheel rims and rail heads. They were machined according to the scheme of Fig. 2, i.e. within the first 30 mm from the surface, with the rolling axis of the specimen perpendicular to the rolling axis of the wheel and to the longitudinal axis of the rail, respectively. The samples were cylindrical with a diameter of 60 mm and a contact track width of 15 mm.

The roughness Ra of the wheel samples was measured before and after the test (0 kcycles and 130 kcycles, respectively). A Mitutoyo SJ 201 rugosimeter has been used and the Ra measurements were accomplished on lines 45° apart along the sample thickness, oriented along X. The measured values are shown in Table 2.

The rolling contact tests were carried out coupling a wheel steel disc as follower, with a rail steel disc as driver under a maximum contact pressure of 1.1 GPa, a rolling speed of 500 rpm and a sliding/rolling ratio of 1%. Before each test the wheel disc was cleaned in a bath of ethanol with ultrasonic vibrations and weighed using a precision balance with a resolution of 0.001 g. The total test duration was 130 kcycles for each couple of specimens; the wheel disk was dismounted at 10 kcycles, 20 kcycles, 30 kcycles, 50 kcycles, 70 kcycles, 100 kcycles and 130 kcycles. At each stop, it was ultrasonically cleaned and weighed to evaluate its weight loss. The experimental curves of the weight loss versus the number of cycles were obtained and the wear rates were calculated.

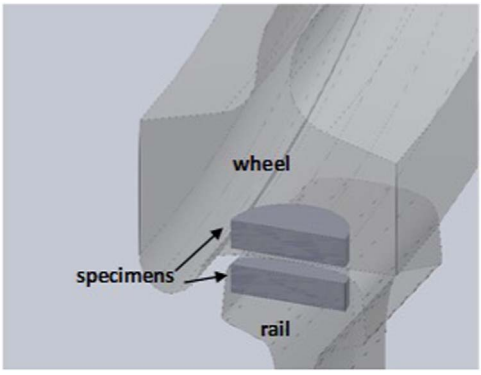

Fig. 2. Section of wheel and rail and of the specimens extracted from them.

Table 2
Roughness Ra (μm) measured on the samples at 0 kcycles and at 130 kcycles.

Steels	0 kcycles		130 kcycles	
	Mean Ra (μm)	ST.Dev Ra (μm)	Mean Ra (μm)	ST.Dev Ra (μm)
CLASS C	1.88	± 0.02	0.72	± 0.10
SANDLOS® S	1.32	± 0.01	0.63	± 0.06
SANDLOS® H	1.96	± 0.03	0.83	± 0.13
ER8	0.93	± 0.04	1.40	± 0.48

2.2. Vision system

The optical layout of the system is shown in Fig. 3a. Point C is the camera entrance pupil, parameter f_l is the lens focal length, and κ is the camera image plane, indexed by c and r for columns and rows respectively. The camera reference system is $\{X_C, Y_C, Z_C\}$, centered at point C, with axis Z_C oriented along the camera optical axis. The specimen S, with diameter D and height H, rotates around axis R. Z_c intersects S at point O, which is the origin of the global reference system {X, Y, Z}. L = $\overline{OC}$ is the stand-off distance. FOVx and FOVy are the dimensions of the Field-of-View along X and Y, respectively: P is a surface point in the FOV.

The image acquisition device is the PROMON 501 – AOS, an 8-bit black and white camera by Technologies AG, operating at frame rates f_c from 85 fps to 3391 fps, at correspondingly decreasing values of the camera resolution; exposure times are software-adjustable from 13 μs to $1/f_c$ [17]. In this study, the camera parameters have been chosen as follows: the acquisition frequency f_c was set to 377 fps, the image resolution was 1280 × 240 px, the exposure time was 40 μs, and the electronic camera gain was 24; the optical focal length was 50 mm. This combination is the optimal one to capture still, good-quality images of disk-shaped specimens with D = 60 mm and H = 15 mm, rolling at 500 fps, with the stand-off distance L = 240 mm, over a FOV of 35 mm × 6.5 mm (FOVx × FOVy). The resulting spatial resolution Rs was 0.027 mm/px, in both X and Y directions.

Fig. 3b schematically shows the illumination geometry. $L_{1,a}$ and $L_{1,b}$ are two laser sources positioned at points A_1 and A_2 with their optical axes along lines a_1 and a_2 respectively. The beams, directed towards point O, are properly defocused to diffusively illuminate the specimen. Coherent light was chosen to provide the best levels of feature visibility and a low signal-to-noise ratio. Semiconductor laser modules (Lasiris™ SNF Laser), emitting 10 mW @ 670 nm, were used. Their emission is polarized, and can be intensity-adjusted by means of a second polarizing filter.

L2 is a laser stripe, which illuminates a purposely-designed analog encoder, denoted by E in Fig. 3. The encoder has a diameter of 50 mm and a linearly varying profile height along the circumference from 3 mm to 8 mm. It is fixed on a disk screwed onto the specimen, and rolls coaxially with the specimen. Fig. 4 shows the vision system integrated with the test bench: W1 and W2 are the twin-disk access windows. W1, whose dimensions are 120 mm × 70 mm, allows to align the optical axis of the camera perpendicularly to the rotation axis of the wheel specimen, and determines the stand-off distance value L. W2, whose dimensions are 120 mm × 100 mm, is aligned at a 135°-angle with respect to W1, and determines the position of the light sources.

As an example, Fig. 5 shows the photograph of the CLASS C sample illuminated by the laser sources (Fig. 5a) and the image captured by the video camera (Fig. 5b).

The diffused laser light impinges on the material and is reflected back to the camera along acquisition directions which depend on the local topography of the surface: the spots visible in the area framed by the rectangular overlay (rectangle 1) present high brightness values and depend on the wear-induced removal of the material; the gray levels framed in the squared overlay (square 2) correspond to background noise and to random speckle patterns induced by the interference of the laser light with the surface at a micro-scale level. The light pattern framed in the rectangular overlay (rectangle 3) is the image of L2: it is viewed as a bright line parallel to X, whose length varies over time depending on the value of the rotation angle.

The apparatus uses, for image acquisition and analysis, a PC (ASUSTeK COMPUTER INC., Processor Intel® Core™ i7-3770 CPU @ 3.40 GHz 3.40 GHz, RAM 8.00 GB), equipped with a dedicated hard disk (SSD 240 GB, Kingston V300 HD) for data storing. Proprietary

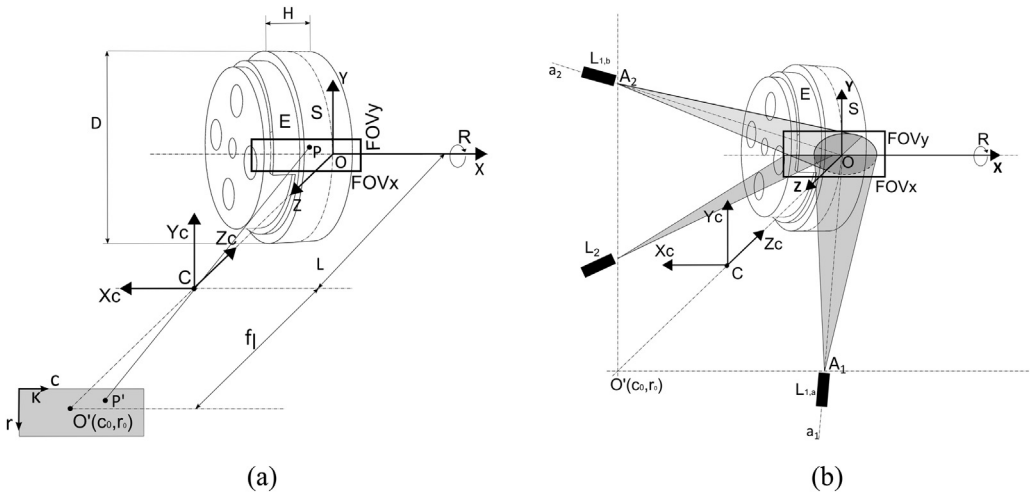

Fig. 3. (a) Optical layout of the system; (b) Geometry of the illumination.

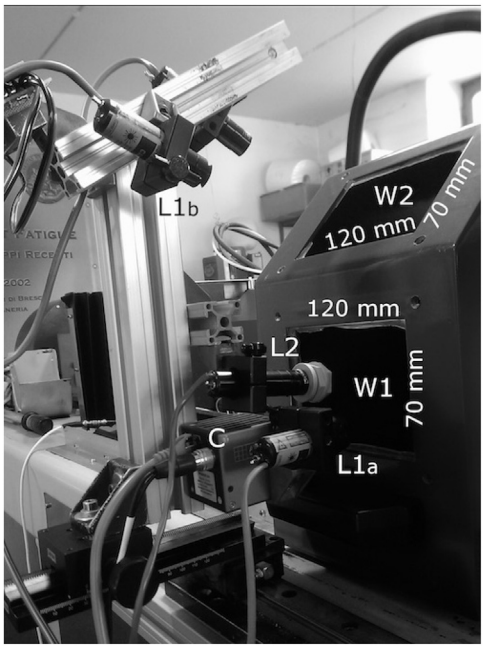

Fig. 4. Vision system assembled on the twin-disk test bench.

software (AOS PROMON Studio) allows the camera parameters selection (resolution, gain, exposure time, pre-triggered interval, acquisition mode). Data storage is carried out by the embedded saving functions of the software, which assemble the frame sequences into suitable video files.

Image acquisition is triggered every 10 s, each acquisition having a duration of 2 s. Each acquired 2-s video consists of N_T = 754 frames subdivided in 16.6 revolutions, each in turn formed by 45.2 frames, (at a rotation speed of 500 rpm and a frame acquisition f_c of 377 fps). Each frame corresponds to a rotation angle of 8°. Univocal relation between frames and angular positions is retrieved analyzing the laser light framed in the rectangle 3 of Fig. 5b as detailed in publication [13]. For the purpose of clarity, here it is sufficient to mention that the line pattern is segmented from the image and that (i) for each image column c, the row position r_G of the center of mass of the gray levels is calculated, (ii) an array of values $\{r_G\}$ is formed, (iii) the array size is calculated and (iv) it is correlated to the value of the rotation angle by means of a suitably developed calibration procedure. The obtained angular resolution is 3° corresponding to 0.26 frames.

We note that the frames partially overlap, due to the constraints imposed by (i) the camera settings, and (ii) the field of view deriving from the camera focal length. To avoid the redundancy in the image analysis, a region of interest is defined on each frame, denoted as ROI1 in Fig. 5b, of dimension 10.3 mm along X and 4.2 mm along Y, and the analysis is limited to that area.

3. Image analysis of ROI1

The light pattern in ROI1 presents bright areas, other than speckles, which are in relation with the surface damage-induced dips. Their evolution in number, dimension and orientation during the tests has been thought of interest for inferring knowledge about the process. The effectiveness of image analysis in damage monitoring is well documented in the literature, mainly in the micro-scale, for texture analysis and roughness measurement. For example, in [18] Gabor filters are proposed for the detection of the image micro-texture, which is related to the particular wear phenomenon under inspection, characterized by repetitive patterns (corrugations). In [19,20] the statistical properties of

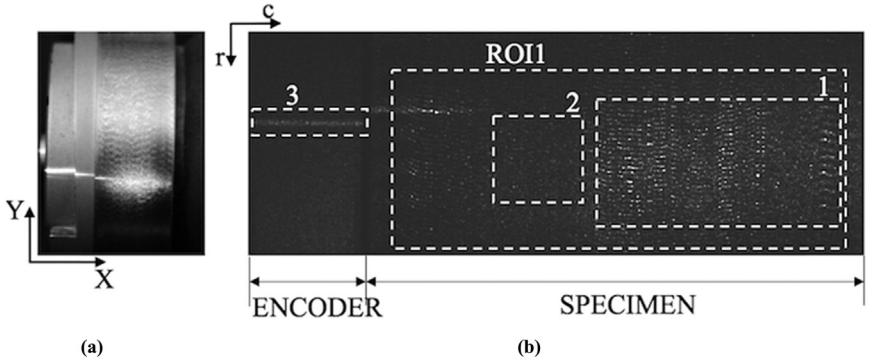

Fig. 5. The illumination/acquisition set-up. (a) CLASS C sample under test and illumination patterns; (b) corresponding image.

binary speckle images are used to measure the surface roughness: suitable thresholding is applied to the image, and dark and bright regions are detected using microscope optics, on a 2 mm^2 area. They are counted and analyzed to establish a correlation between the measured quantities and the roughness parameters. In recent times, advanced image analysis based on neural networks and support vector machines has been proposed as a valuable approach for damage classification [21]. In our application, however, the analysis focuses on FOVs larger than those typical of roughness investigations, and the patterns are non-texturized; although pattern classification using machine learning is certainly of interest, at the present step of development it is not suitable, as it requires time crunching image collection in data-bases and network training. Thus, a simpler approach, which takes inspiration from publication [19] has been chosen, where bright regions are segmented from the background using thresholding and are processed using specific particle analysis algorithms, able to identify connected pixels in the binary image (the particles) and to provide information on their number and morphology [22]. Both image thresholding and particle analysis have been developed using the IMAQ vision image processing suite of functions, in the LabView framework [23].

3.1. Image thresholding

Image thresholding is performed by comparing the gray-level of each analyzed pixel to a threshold value, and by substituting this value with 0 (black) or 1 (white) if the threshold is higher or lower than the pixel value respectively. The choice of the threshold is critical, and many algorithms, based on global or local thresholds, either selected by the user or calculated using suitable image indicators, are available [24]. In our system, the value of the threshold is set to eliminate the gray levels of the background (where the signal-to-noise ratio is very low) from the image. The background information is expected to be constant during the tests, as it depends on the system illumination which does not change from 0 cycles to 130 kcycles. The histograms of the images taken at 0 cycles typically show a single, narrow lobe, whose peak position depends on the illumination intensity and on the steel reflectivity at 0 cycles. In our procedure, we first compute the cumulative mean histogram calculated over the images of the video captured before starting the test (i.e., at 0 cycles) for each steel, and then we set the threshold value as the gray level corresponding to the last percentile of the cumulated histogram. This value is used to threshold all the frames captured during the whole test, and guarantees that the residual information retained in the images depends only on the damage process.

As an example, in Fig. 6 we present the effect of this procedure applied to the CLASS C steel. Fig. 6a and b present the image portions framed by rectangle 1 and by square 2 in the image of Fig. 5b respectively: bright pixels are well separated from a black background, and both the image signal-to-noise ratio and contrast are improved.

3.2. Particle analysis

Particle analysis in binary images focuses on the detection of connected pixels, referred to as particles. A typical particle analysis process scans through an entire image, detects all the particles in the image, and builds a detailed report on each particle, listing the values of multiple parameters such as the number of pixels in the particle, the area of the particle, the pixel coordinates of the center of gravity, and the orientation of the particle. Suitable algorithms [25] perform selective particle filtering, to eliminate particles that are of no interest based on their spatial characteristics, and keep only the relevant particles for further analysis. As a first step, we used particle filtering to eliminate from the image all the particles formed by a single pixel: this operation has been performed to minimize residual speckles, which are not relevant for the investigation.

As a second step, we studied the changes of the particle characteristics during the tests, with the aim of correlating them to the evolution of the damage process. To clearly explain our approach, we refer to the images shown in Fig. 7 taken during the test carried out on the CLASS C steel, just before dismounting the sample for measuring its weight loss. The figure shows, from left to right, (i) the photograph of the surface under observation corresponding to a pre-predefined angular position, (ii) the particle pattern in the ROI and (iii) the zoom-in of the pattern. From these images, it can be observed that the number of particles varies during the test: it reaches its maximum in the image at 10 kcycles and gradually decreases in the subsequent images. In addition, the particles change their shape: they are round-shaped at 50, 100 and 130 kcycles, whilst they are elongated in the Y direction at 10 and 70 kcycles, and in the X direction at 20 and 30 kcycles. Finally, the particles in the images at 10, 20 and 30 kcycles are larger than those in the other images, and elongated particles appear larger than round-shaped particles. Based on these observations, we analyzed the following particle parameters: their number, their shape, and their area.

3.2.1. Particle number

The particle number has been evaluated grouping particles in classes according to their areas in px. The grouping is consistent with [13]. Table 3 lists the area ranges defined as (i) very small, (ii) small, (iii) medium, (iv) large, and (v) very large.

The particle number has been measured by summing up the number of the particles belonging to the i-th class (i = 1,…5) in each frame and by averaging the result over the number N_T of frames in each analyzed 2-s video. The resulting index is called N_i.

3.2.2. Particle shape

The particle shape has been measured using the particle analysis function that calculates the so-called roundness factor, by framing each particle within a rectangle and by forming the ratio a_s between the height and the width of the rectangle. If $a_s > 1$ the particle is oriented along the vertical direction Y, if $a_s < 1$ the particle is oriented along the horizontal direction X, and if $a_s = 1$ the particle is round-shaped. For each frame, values a_s were calculated for each class and averaged over

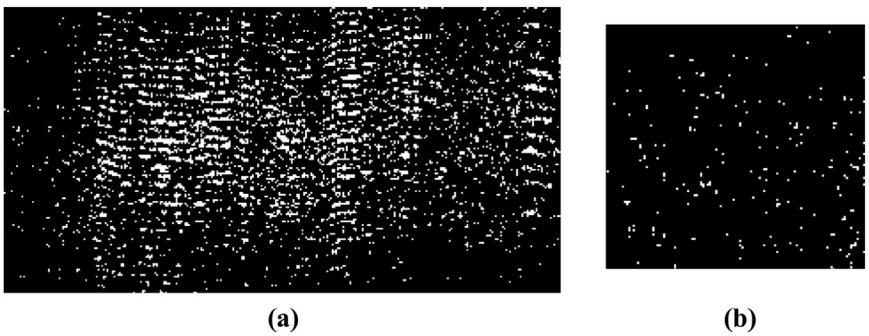

(a) (b)

Fig. 6. Effect of the thresholding applied to the image in Fig. 5b. (a) Image framed by the overlay 1; (b) image framed by overlay 2.

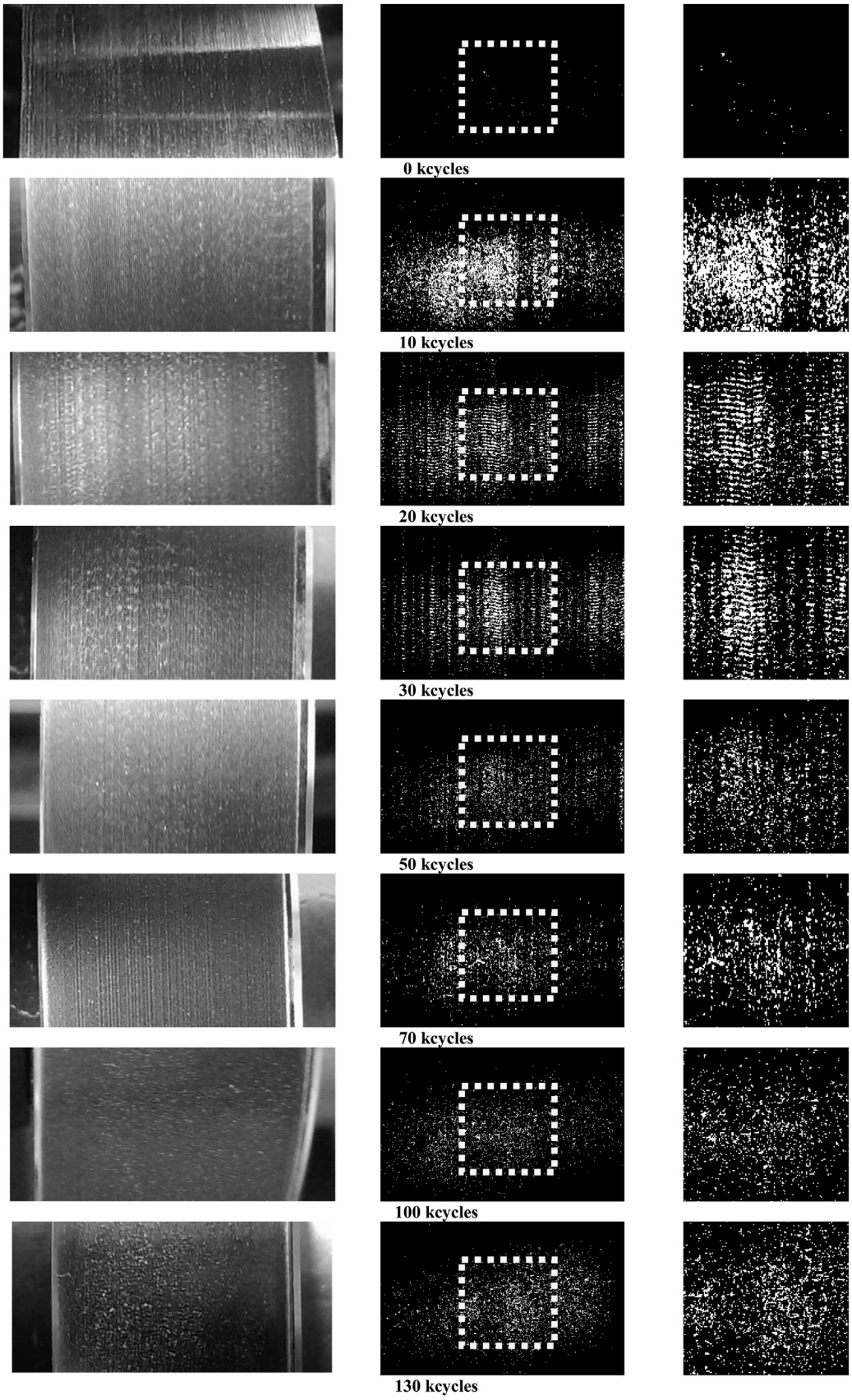

Fig. 7. Images taken during the test of CLASS C. Left column: photographs of the sample; central column: particle patterns; right column: zoom-in of the particle patterns.

Table 3
Classification of the particles.

Class	Area range [pixel]
C_1 (very small)	2–5
C_2 (small)	6–15
C_3 (medium)	16–30
C_4 (large)	31–70
C_5 (very large)	> 70

the number of particles in that class. Then, the average value $A_{s,i}$ over the N_T frames in each video was obtained.

3.2.3. Particle area

The particle area was taken into account to measure quantitatively the variation of the percentage of the area occupied by the particles "as a whole" with respect to the area of the ROI, against the number of cycles (all the measurements are in pixels). This index has been calculated as follows: for each frame, the total area of the particles was computed and divided by the area of ROI1; then the average value of this ratio was evaluated (i) over the total number N_T of frames, and (ii) over a subset of frames, i.e., considering only those frames at specific angular positions. In the following, this parameter will be referred to as the damage ratio R, meaning that, in the hypothesis that bright spots are related to the removed material, it is a measure of the sample damage.

4. Experimental results

4.1. Weight loss

The plots of the weight loss versus the number of cycles of the tested steel are shown in Fig. 8. The curves show an initial incubation period, lasting 10 kcycles for CLASS C, 30 kcycles for SANDLOS S, 20 kcycles for SANDLOS H and 30 kcycles for ER8. After this period, all the plots show a steady state period, where the weight loss is linear, corresponding to constant wear. The wear rate calculated in the steady-state period of the wear curves is also shown in each plot. ER8 shows higher weight loss and wear rate than the other three steels because of its lower hardness. These values are in accordance with the weight loss and wear rate obtained in a different set of tests performed on the same steels under the same experimental conditions, recently published in [26] (see the test "without sand"). In that study the behavior of the steels was evaluated also in terms of strain hardening, surface and subsurface damage: this set of measurements has not been performed in this work, since we thought it reasonable that the steels tested in the study presented in this paper underwent the same damage process as the one in [26]. The behavior of the wear curves in Fig. 9 is well documented in the literature. In fact, it is well-known that, during twin-disk tests, the wear phenomenon exhibits two experimentally recognizable stages: an early stage, with transient wear-rate, and a consequent steady-state stage, with quasi-stable wear-rate [27,28]. In the

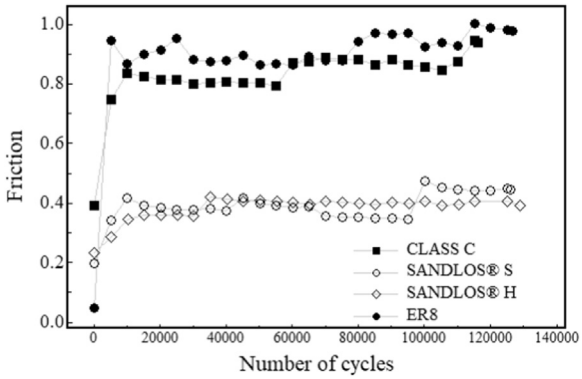

Fig. 9. Evolution of the friction coefficients as a function of the number of cycles.

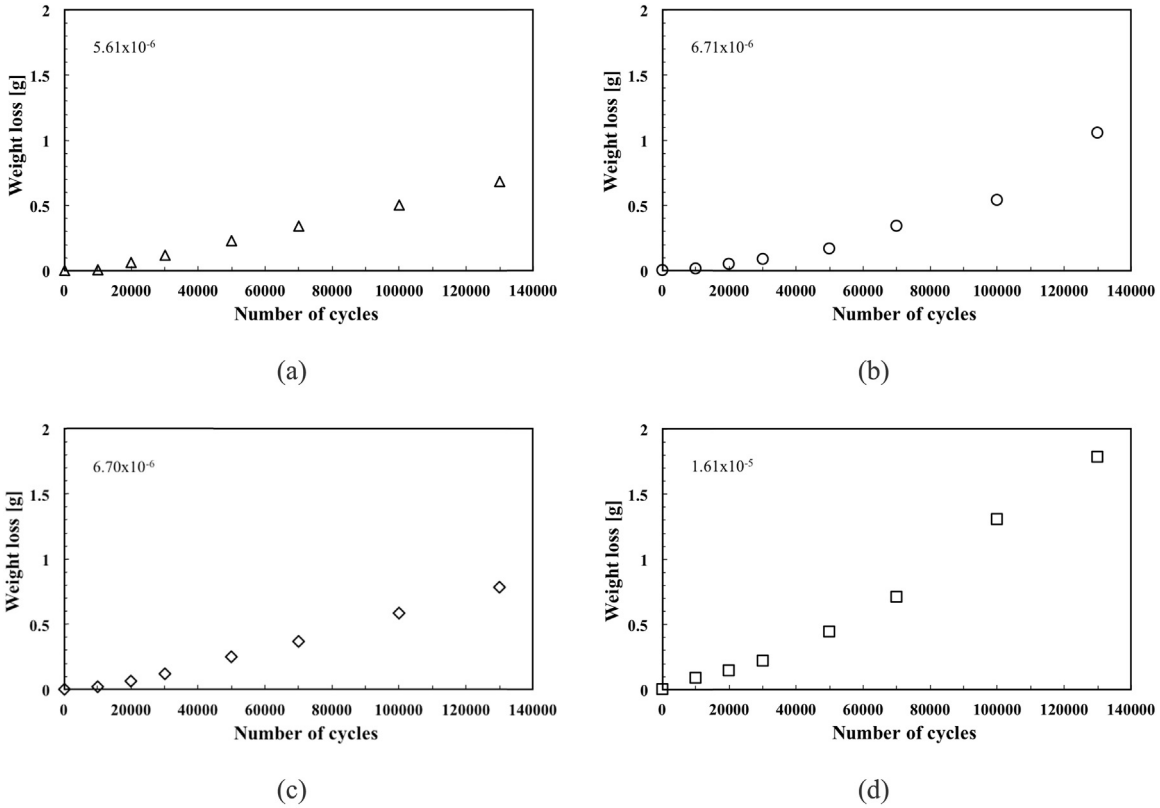

Fig. 8. Experimental curves of the weight loss versus the number of cycles and wear rate [g/cycle] for the tested steels. (a) CLASS C; (b) SANDLOS® S; (c) SANDLOS® H; (d) ER8.

former stage, the turning-crests of the rolling surfaces are removed. In the latter, wear and RCF processes are in competition with each other: wear continuously removes surface material layers and flattens out the product of RCF (that is, the formation of cracks) [29].

4.2. Friction coefficients

The friction coefficients measured during the tests are plotted in Fig. 9. They are grouped in two separate sets: the former includes ER8 and CLASS C, the latter SANDLOS® S and SANDLOS® H. In both sets, the values of the coefficients after 10 kcycles are almost constant, but with markedly different values, which are doubled in the former set with respect to the latter.

4.3. Indices measured by the vision system

In this section the indices measured by the vision system are presented. The measurements have been computed using the videos captured every 5 min from 0 cycles to 30 kcycles, every 10 min from 30 kcycles to 70 kcycles, and every 12 min from 70 kcycles to 130 kcycles. The steps in the 0–30 kcycles are denser than the others because we wanted to carefully study the test phase where the weight curves are non linear; the steps chosen for the measurements in the 30–70 kcycles and in the 70–130 kcycles are a reasonable trade off between the significance of the data and the elaboration time.

4.3.1. Indices measured on CLASS C

The elaboration carried out on the specimen made of CLASS C resulted in the plots shown in Fig. 10. The behavior of index N_i is presented in two separate plots (for clarity purposes): the plot in Fig. 10a refers to classes C_1 and C_2, and the plot in Fig. 10b refers to classes C_3 - C_5. N_1 and N_2 are much greater than N_3, N_4 and N_5; however, all the indices share the same behavior, with increasing values from 0 cycles to 20 kcycles and decreasing values from 20 kcycles to 50 kcycles (N_2 - N_5) and to 60 kcycles (N_1). At higher number of cycles, the indices are substantially stable until the test end. During the test evolution, only very small and small particles persist, while the number of larger particles is negligible: this is in accordance with the patterns observed in Fig. 7.

The asymmetry index $A_{s,i}$ is shown in Fig. 10c for each class. The particles gradually change their shape during the test; very small particles become elongated along the Y direction at 10 kcycles, are round-shaped from 20 kcycles to 40 cycles, undergo a deformation along Y at 70 kcycles, and become round shaped at higher numbers of cycles. The other particles substantially follow the same behavior, with the exception of the 12.5–30 kcycles, where they are horizontally oriented. This behavior finds its counterpart in the images at 10 Kcycles, 20 kcycles and 30 kcycles shown in Fig. 7.

Index R is presented in Fig. 10d: its value rapidly increases at the beginning of the test, reaches its maximum at 10 kcycles, and decreases to a plateau region starting at 40 kcycles. In this region R values are about 2%.

4.3.2. SANDLOS® S

The elaboration carried out on the specimen made of SANDLOS® S resulted in the plots shown in Fig. 11.

The number of particles (Fig. 11a and b) increases from 0 to 20 kcycles for all the classes. The particle number N_1 does not significantly vary until 30 kcycles, then decreases of about 50% at 40 kcycles and remains almost constant until 130 kcycles. All the remaining particles rapidly decrease to very low values after 30 kcycles. At higher cycles, the indices are substantially stable until the test end. During the test evolution, only very small and small particles persists, while the number of larger particles is negligible.

Fig. 11c plots the behavior of the particle shape: the particles belonging to classes from C_2 to C_5 are elongated along X at 20 and at 30 kcycles. With the evolution of the process, most particles become round-shaped (note that the value of index $A_{s,3}$ refers to a very low number of particles, so that their influence is negligible).

Index R (Fig. 11d) shows a behavior very similar to the one

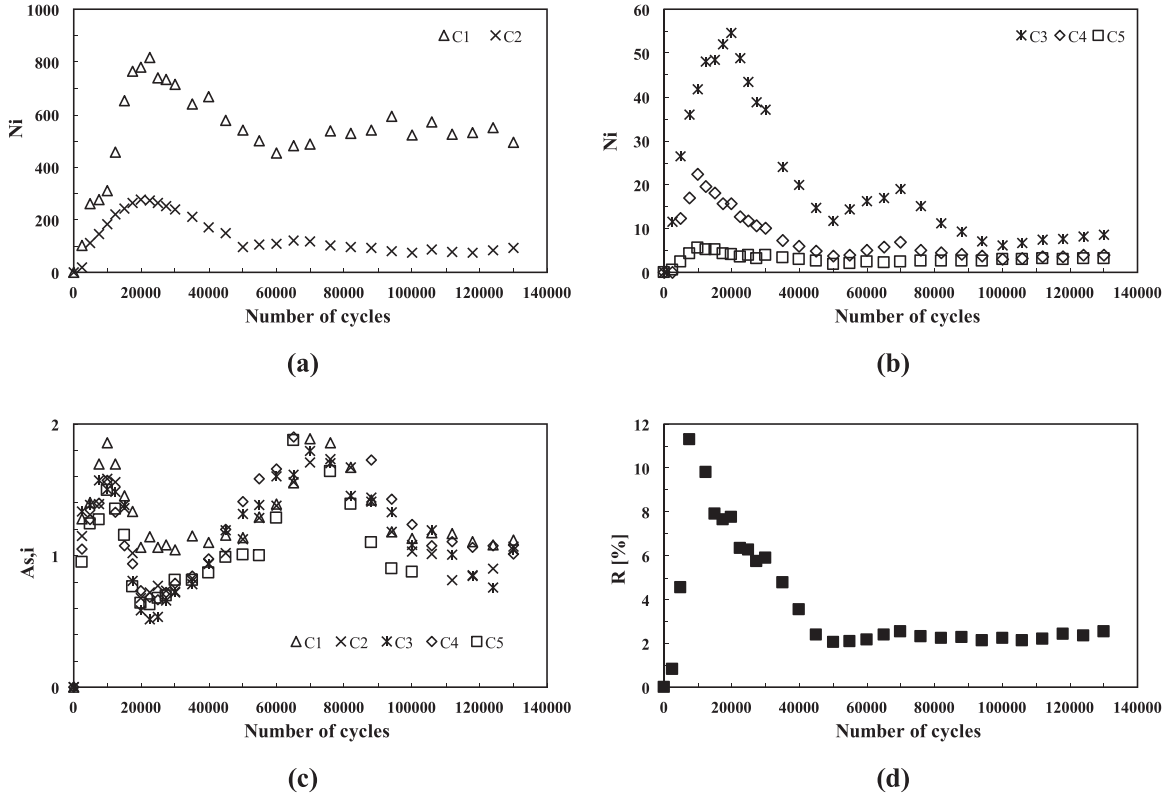

Fig. 10. Evolution of indices N_i $A_{s,i}$ and R with the number of cycles for CLASS C; (a) indices N_1 and N_2; (b) indices from N_3 to N_5; (c) index $A_{s,i}$; (d) index R.

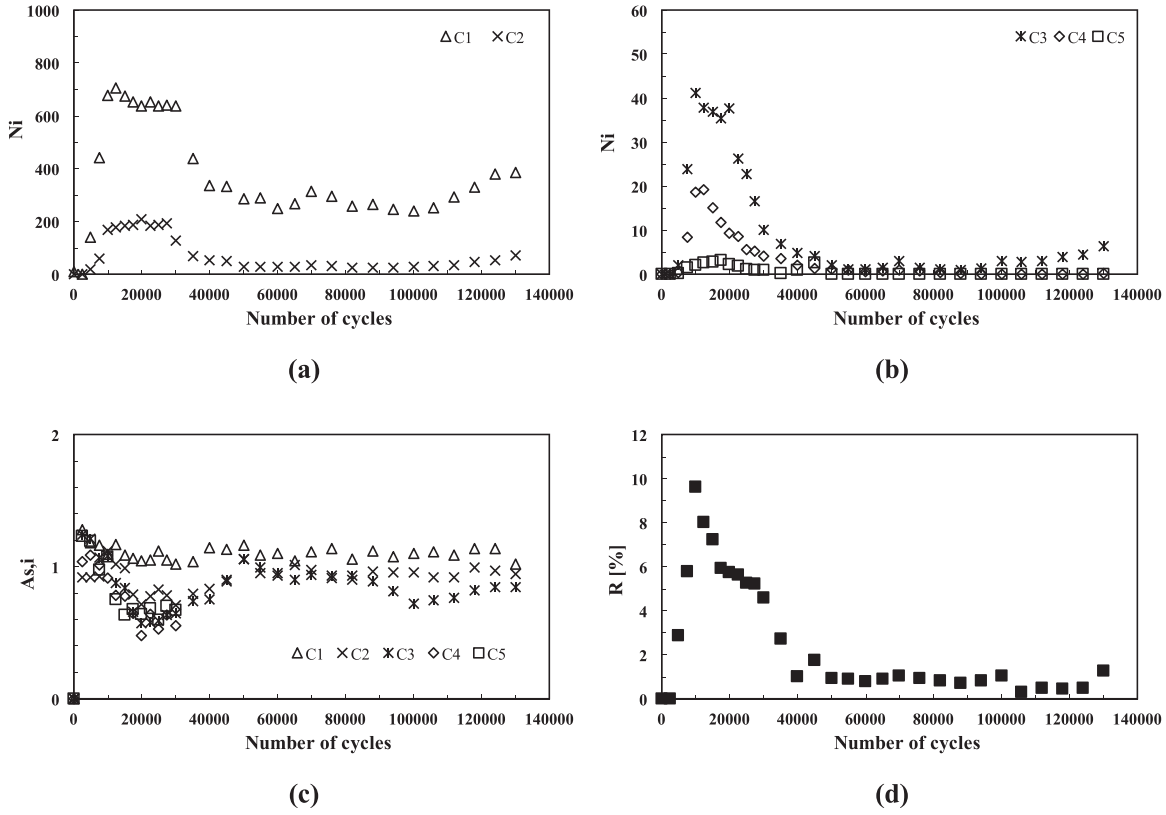

Fig. 11. Evolution of indices N_i $A_{s,i}$ and R with the number of cycles for SANDLOS® S; (a) indices N_1 and N_2; (b) indices from N_3 to N_5; (c) index $A_{s,i}$; (d) index R.

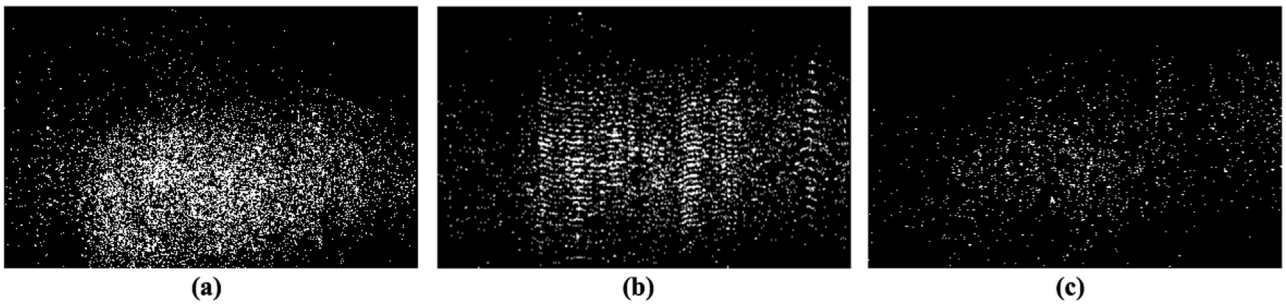

Fig. 12. Particle appearance at 10 kcycles (a), 20 kcycles (b) and 50 kcycles (c) for SANDLOS® S.

observed for the CLASS C steel, characterized by a steep increment to its peak value of 9,7% at 10 kcycles, and by a decrease to a bottom plateau region from 40 kcycles to 130 kcycles. In this region, R values are below 1%.

The behavior of the indices in Fig. 11 finds a correlation with the visual appearance of the patterns in the images in Fig. 12, captured at 10, 20 and 50 kcycles respectively. The particles are characterized by the presence of many round-shape particles at 10 kcycles, of elongated particles at 20 kcycles and of a reduced number of small round-shape particles at 50 kcycles.

4.3.3. SANDLOS® H

The elaboration performed on the specimen made of SANDLOS® H resulted in the indices shown in Fig. 13. The evolution of the particle number N_i (Fig. 13a and b) is similar to those described above; however, the plateau region is observable from 30 kcycles for all the classes with the exception of class C_1, which stabilizes after 70 kcycles. The asymmetry index (Fig. 13c) does not reveal significant elongations of the particles, as particles belonging to classes C_3 and C_4 are very few. Index R (Fig. 13d) shows the same trend as in the steels above, with the peak value at 5 kcycles, and the plateau region starting after 30 kcycles. These observations are in accordance with the images in Fig. 14, which show the particle patterns at 10 kcycles (Fig. 14a) and at 30 kcycles (Fig. 14b).

4.3.4. ER8

The elaboration carried out on the specimen made of ER8 resulted in the indices shown in Fig. 15. Index N_i (Fig. 15a and b) still presents a dependence on the number of cycles, but it is less evident than in the other specimens. The asymmetry index (Fig. 15c) does not reveal significant changes in the particle shape. Index R (Fig. 15a) reaches its peak value at 10 kcycles and decreases at increasing number of cycles, like in the materials previously presented; however, the descending slope is lower than for the other steels. These observations can be confirmed by looking at the images in Fig. 16, which present the particle patterns acquired at 10 kcycles (Fig. 16a) and at 30 kcycles (Fig. 16b).

5. Discussion

In all the tested steels, R values are negligible at 0 kcycles, reach the peak value at the beginning of the tests, then decrease with a material-

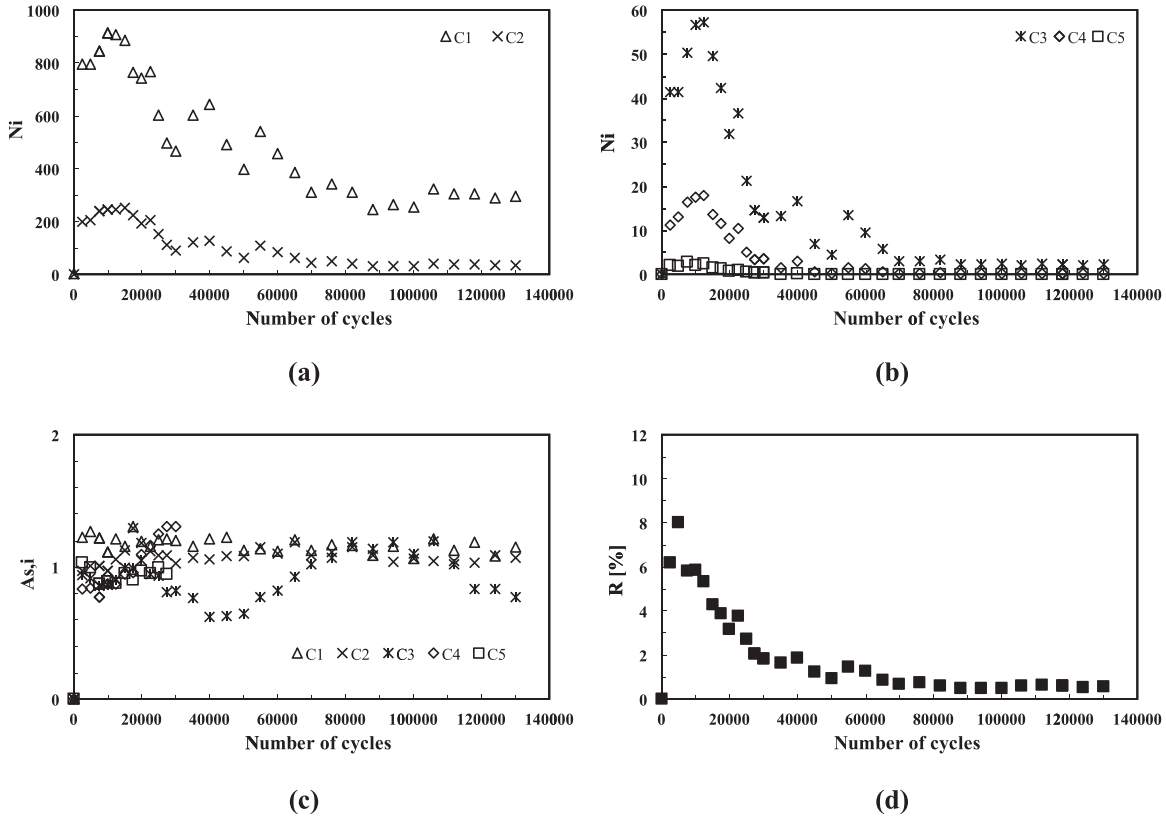

Fig. 13. Evolution of indices N_i $A_{s,i}$ and R with the number of cycles for SANDLOS® H; (a) indices N_1 and N_2; (b) indices from N_3 to N_5; (c) index $A_{s,i}$; (d) index R.

dependent slope and, from a certain point thereafter, they remain almost constant until the end of the test.

This behavior can be correlated to the two stages observed from the weight loss curves in Section 4.1: in the early stage, with transient wear-rate, R increases rapidly and in the subsequent steady-state stage, R is almost constant, consistently with the quasi-stable wear-rate. This hypothesis is further supported by the analysis of the evolution of the class-specific number of particles N_i. In the peak region, the number of the particles is very high, which can be correlated to the material removal induced by the wear process; in the flattened region, however, (i) the particle number decreases, (ii) it does not undergo significant variations with the number of cycles and, more important, (iii) only small particles are observable. In this case, the wear-induced material removal prevents the formation of larger particles, corresponding to the material detachment due to the propagation of the fatigue-induced cracks.

The analysis presented above is also helpful to highlight the differences among the tested steels. Firstly, the steels differ in the values of R in the steady-state stage. In particular, ER8 shows the highest R values in this region, and this can be correlated to its highest wear rate from the weight loss measurements, which is due to its lower hardness with respect to the other steels. As shown in Table 1, ER8 is the softest steel, and it undergoes the greatest damage at the contact surface.

In addition, the values of R in the steady state can be grouped in two sets, with values of R always higher for ER8 and CLASS C with respect to the SANDLOS-type steels. This characteristic finds its counterpart in the friction coefficients of the steels shown in Fig. 9, which are grouped in two separate sets, the former including ER8 and CLASS C, the latter SANDLOS® S and SANDLOS® H.

Secondly, the transition between the two stages is material-dependent. This observation is supported by the behavior of the asymmetry index $A_{s,i}$: in CLASS C and SANDLOS® S, the particles are initially small and round shaped. Then they become larger and elongated. This observation is consistent with the onset of unidirectional friction of the contact surfaces with an induced plastic flow, which results in the formation of corrugations, already observed and documented in past experiments [11]. In contrast, SANDLOS® H and ER8 are characterized by asymmetry indices close to 1 during the whole tests duration, and, consistently with this quantitative measure, they do not present corrugations.

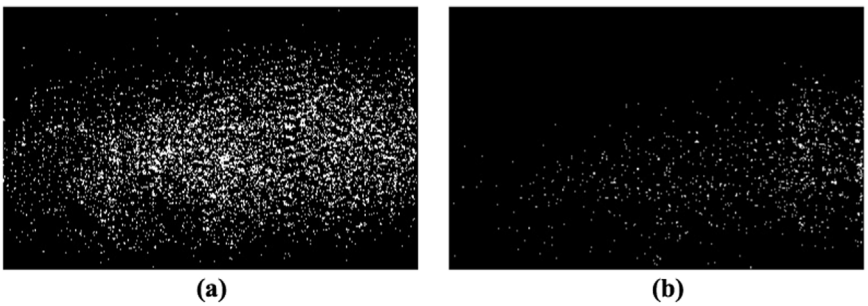

Fig. 14. Particle appearance at 10 kcycles (a) and at 30 kcycles for SANDLOS® H.

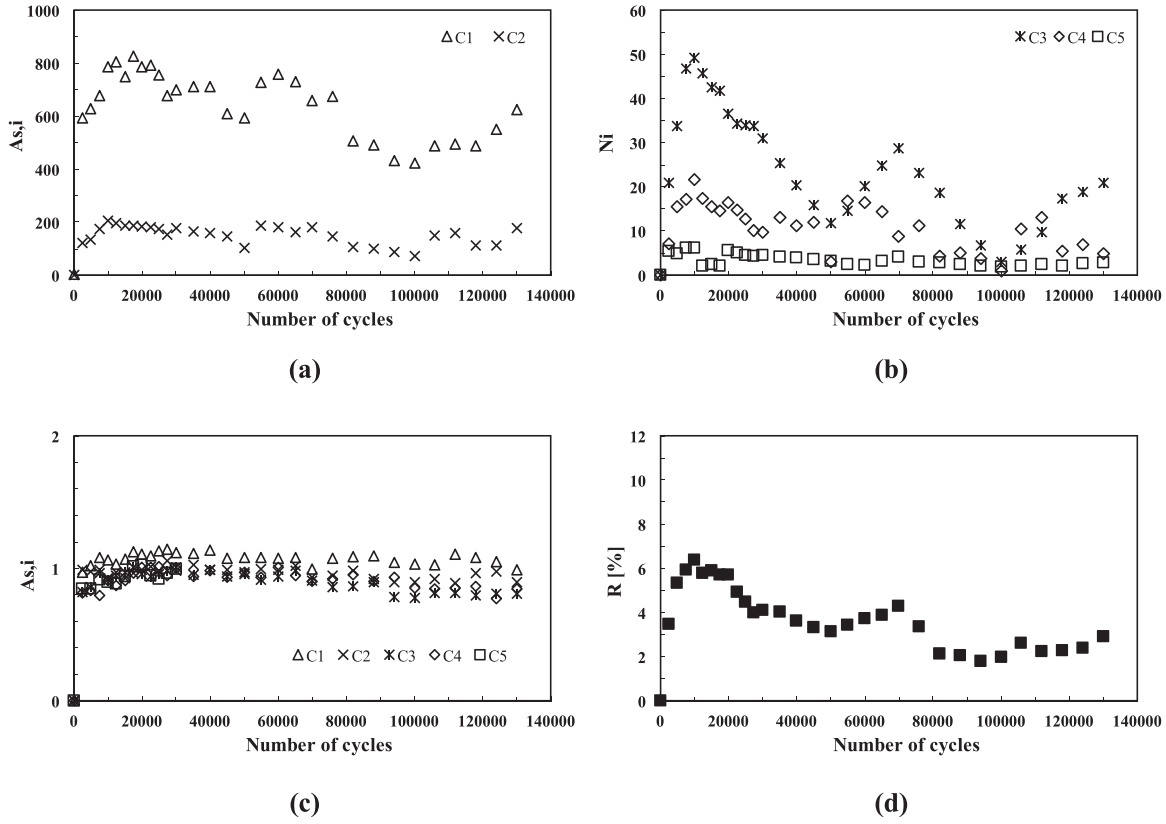

Fig. 15. Evolution of indices N_i $A_{s,i}$ and R with the number of cycles for ER8; (a) indices N_1 and N_2; (b) indices from N_3 to N_5; (c) index $A_{s,i}$; (d) index R.

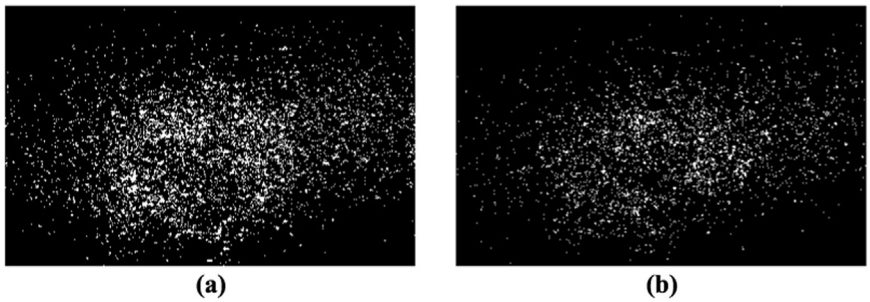

Fig. 16. Particle appearance at 10 kcycles (a) and at 50 kcycles for ER8.

6. Detection of uneven wear

A unique advantage of the optical system is its ability to monitor the temporal evolution of a disk under test on an angle-dependent basis. This makes it possible to identify and measure non-uniform damage of the rolling specimen. As an example, we present the analysis carried out on the disk shown in Fig. 17: this specimen is made of UIC 900A, which is rail steel. It underwent an 800 kcycles-long dry test against a wheel-specimen made of Superlos®, and became polygonal during the test. The visual inspection of this sample reveals that the surface is characterized by an alternation of regions at different reflectivity, related to the local amount of wear: in particular, the reflectivity decreases in the regions where the wear damage is higher. The image of Fig. 18a has been obtained by stitching 45 frames acquired every 8°, corresponding to a rotation of 360° of the sample; each frame is labelled by its number in the acquisition sequence. The linear profile of the encoder is visible above the sample surface, and the angular values from 0 to 360 are graphically drawn at steps of 90°. Fig. 18b shows index R calculated over each single frame for three consecutive revolutions. Index R is very low in frames corresponding to high reflectance of the surfaces (uniformly dark frames), where low wear is observed, as in frames 1, 2, 6, 7, 20, 21, 24, 25, 28, 29, 30, 41 and 42. In contrast, the values of R increase above 3% in frames at reduced reflectivity (showing a predominance of lighter gray levels), where the wear yields uniform damage of the surface, as in frames 4, 8, 27, 44. In the remaining frames, corrugations are visually observable, resulting in intermediate values of

Fig. 17. Surface appearance of the specimen affected by polygonalization.

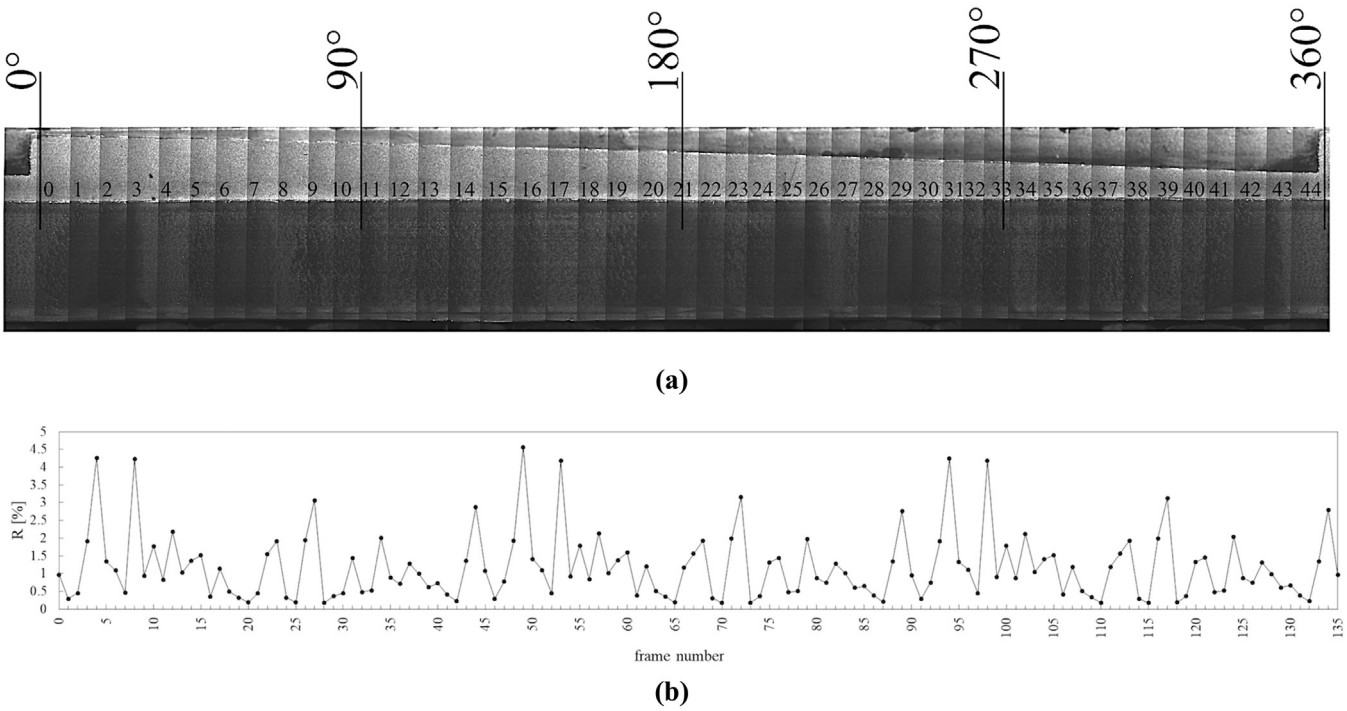

Fig. 18. Polygonalization effect. (a) Stitching of the frames acquired along the whole circumference of the sample; (b) plot of index R corresponding to each frame.

R. The plot of R is repeatable over subsequent revolutions (in Fig. 18b three revolutions are shown). This high, repeatable variability of R can be quantitatively detected, for example by monitoring the dynamics of index R using a threshold-based approach or by calculating its deviation from the mean value on a moving-window interval, and can be used as an evidence of uneven wear as a consequence of incorrect specimen mounting, which should force the test stop.

7. Conclusions

In this paper the results of the experiments carried out to extract quantitative information from the images acquired on railway wheel samples during dry rolling contact tests have been presented. Both the vision system used for acquiring the images and the image analysis approach have been reported. A set of synthetic indices has been proposed as a valuable mean to give a quantitative measure of the wear process and a comparative analysis has been carried out on samples of different steels, to assess the significance of the indices in relation to (i) known phenomena, such as the existence of transient and steady stages in the evolution of wear, (ii) material properties, such as hardness, (iii) plastic flow-induced corrugations.

The results are encouraging, and show that the two test methods yield the same information with the great advantage of our system to be able to derive this information without intermediate sample removal and cleaning. They can lead to the development of on-line image analysis, aimed at detecting and storing only those events that are meaningful either for the understanding of the material properties or for the monitoring of the test bench. Further activity is being developed in long duration, wet tests, characterized by fatigue–induced damage, to understand how the proposed indices behave and if they can be correlated to fatigue phenomena besides wear, for early interruption of the tests and sample post mortem analysis.

Acknowledgements

We wish to thank Mr. Gabriele Coffetti and Mr. Silvio Bonometti for their precious support in the experimental activities.

References

[1] A. Ekberg, E. Kabo, Fatigue of railway wheels and rails under rolling contact and thermal loading – an overview, Wear 258 (7–8) (2005) 1288.
[2] A. Mazzù, C. Petrogalli, M. Faccoli, An integrated model for competitive damage mechanisms assessment in railway wheel steels, Wear 322–323 (2015) 181.
[3] W.J. Wang, R. Lewis, B. Yang, L.C. Guo, Q.Y. Liu, M.H. Zhu, Wear and damage transitions of wheel and rail materials under various contact conditions, Wear 362–363 (2016) 146.
[4] J. Wei, A.Q. Zhang, P. Gao, A study of spur gear pitting under EHL conditions: theoretical analysis and experiments, Tribol. Int. 94 (2016) 146.
[5] U. Olofsson, T. Telliskivi, Wear, plastic deformation and friction of two rail steels – a full scale test and a laboratory study, Wear 254 (2003) 80.
[6] C. Kammerhofer, A. Hohenwarter, R. Pippan, A novel laboratory test rig for probing the sensitivity of rail steels to RCF and wear – first experimental results, Wear 316 (2014) 101.
[7] D.I. Fletcher, S. Lewis, 2013. Creep Curve Measurement to Support Wear and Adhesion Modelling, Using a Continuosly Variable Creep Twin Disc.
[8] G. Donzella, M. Faccoli, A. Ghidini, A. Mazzù, R. Roberti, The competitive role of wear and RCF in a rail steel, Eng. Fract. Mech. 72 (2) (2005) 287.
[9] G. Donzella, M. Faccoli, A. Mazzù, C. Petrogalli, R. Roberti, Progressive damage assessment in the near-surface layer of railway wheel-rail couple under cyclic contact, Wear 271 (1–2) (2011) 408.
[10] M. Lancini, I. Bodini, D. Vetturi, S. Pasinetti, A. Mazzu`, L. Solazzi, C. Petrogalli, M. Faccoli, Using vibration measurements to detect high wear rates in rolling contact fatigue tests, ACTA IMEKO 4 (4) (2015) 66.
[11] A. Mazzù, L. Solazzi, M. Lancini, C. Petrogalli, A. Ghidini, M. Faccoli, An experimental procedure for surface damage assessment in railway wheel and rails steels, Wear 342–343 (2015) 22.
[12] M. Meywerk, Polygonalization of railway wheels, Arch. Appl. Mech. 69 (1999) 105.
[13] I. Bodini, G. Sansoni, M. Lancini, S. Pasinetti, F. Docchio, A novel optical apparatus for the study of rolling contact wear/fatigue based on a high-speed camera and multiple-source laser illumination, Rev. Sci. Instrum. 87 (8) (2016) 083701.
[14] I. Bodini, G. Sansoni, M. Lancini, S. Pasinetti, F. Docchio, Feasibility study of a vision system for on-line monitoring of rolling contact fatigue tests, J. Phys.: Conf. Ser. 778 (2017) 012007.
[15] G.A. Al-Kindi, B. Shirinzadeh, An evaluation of surface roughness parameters measurement using vision-based data, Int. J. Mach. Tools Manuf. 47 (2007) 697.
[16] B. Dhanasekar, B. Ramamoorthy, Assessment of surface roughness based on super resolution reconstruction algorithm, Int. J. Adv. Manuf. Technol. 35 (11–12) (2008) 1191.
[17] Datasheet PROMON 501 available at 〈http://www.aostechnologies.com/〉.
[18] J. Zhang, M. Korsten, P. Regtien. A vision system for online wear detection, in: Proceedings of the XVII Imeko World Congress, June 22–27, Dubrovnik, Croatia, p. 1960.
[19] E. Kayahan, H. Oktem, F. Hacizade, H. Nasibov, O. Gunogdu, Measurement of surface roughness of metal using binary speckle image analysis, Tribol. Int. 43 (2010) 307.
[20] Y.-K. Fuh, K.C. Hsu, J.R. Fan, Roughness measurement of metal using a modified

binary speckle image and adaptive optics, Opt. Laser Eng. 50 (2012) 312.
[21] G. Samtas, Measurement and evaluation of surface roughness based on optic system using image processing and artificial neural network, Int. J. Adv. Manuf. Technol. 73 (1–4) (2014) 353.
[22] T.B. Moeslund, Introduction to Video and Image Processing – Building Real Systems and Applications (Undergraduate Topics in Computer Science), Springer Verlag, **London**, 2012, p. 103.
[23] T. Klinger, Image Processing with LabVIEW and IMAQ Vision, Prentice Hall Professional, **New Jersey**, 2003, p. 5.
[24] M. Sezgin, B. Sankur, Survey over image thresholding techniques and quantitative performance evaluation, J. Electron. Imaging 13 (1) (2004) 146.
[25] T. Klinger, Image Processing with LabVIEW and IMAQ Vision, Prentice Hall Professional, **New Jersey**, 2003, p. 4.
[26] M. Faccoli, C. Petrogalli, M. Lancini, A. Ghidini, A. Mazzù, Effect of desert sand on wear and rolling contact fatigue behaviour of various railway wheel steels, Wear (2017), http://dx.doi.org/10.1016/j.wear.2017.05.012.
[27] B. Bhushan, Modern Tribology Handbook, 1 CRC Press, Boca Raton, 2000, p. 7.
[28] J.F. Archard, Contact and rubbing of flat surfaces, J. Appl. Phys. 24 (1953) 981.
[29] G. Donzella, A. Mazzù, C. Petrogalli, Competition between wear and rolling contact fatigue at the wheel-rail interface: some experimental evidence on rail steel, Proc. Inst. Mech. Eng. Part F: J. Rail Rapid Transit 223 (1) (2009) 31.